Damage of woven composite under tensile and shear stress using infrared thermography and micrographic cuts

Teddy Lisle, Christophe Bouvet, Marie-Laetitia Pastor, Thomas Rouault, Philippe Marguerès

Damage of woven composite under tensile and shear stress using infrared thermography and micrographic cuts

T. Lisle[1] · C. Bouvet[1] · M. L. Pastor[1] · T. Rouault[2] · P. Margueres[1]

Abstract Infrared thermography was used to study damage developing in woven fabrics. Two different experiments were performed, a ±45° tensile test and a rail shear test. These two different types of tests show different damage scenarios, even if the shear stress/strain curves are similar. The ±45° tension test shows matrix hardening and matrix cracking whereas the rail shear test shows only matrix hardening. The infrared thermography was used to perform an energy balance, which enabled the visualization of the portion of dissipated energy caused by matrix cracking. The results showed that when the resin is subjected to pure shear, a larger amount of energy is stored by the material, whereas when the resin is subjected to hydrostatic pressure, the main part of mechanical energy is dissipated as heat.

Introduction

Because of the complex inhomogeneous microstructure, the weave architecture and disparate meso-constituent properties, the failure process of woven composite is complex and involves a multitude of fracture modes (matrix cracking, inter-yarn and intra-yarn cracking, inter-ply and intra-ply delamination). For the past decades, several authors have investigated the damage scenario of different woven composite laminates under quasi-static tensile loading [1–5]. For woven carbon- and glass-fibre-reinforced composites, transverse yarn cracking is the first readily observable type of damage occurring during tensile loading. As the strain increases, damage develops on the meso-scale by intra-yarn cracking and delamination, and on the micro-scale by local debonding at the fibre–matrix interface as reported by John et al. [2]. The final macro-fracture is characterized by dense cracking, intersection of several small cracks and fibre rupture.

In order to study the complex damage scenario of woven composite, traditional techniques such as X-ray, ultrasound C-scan imaging, acoustic emission, or digital image correlation may be insufficient and thermography can provide interesting additional information. Moreover, the thermography technique provides an energy-related information that can be used to characterize the irreversible energy dissipated, like the fracture toughness [6–9]. Nevertheless in order to evaluate this dissipated energy quantitatively, the ratio of energy dissipated as heat to irreversible energy, i.e. the Taylor–Quinney coefficient [10], is needed, and it can be difficult to evaluate this coefficient [11, 12].

This paper offers a specific analysis of damage mechanisms in thin woven composites. It remains complex to predict damage and durability in structures made of such materials particularly with defects. For example, a notch induces stress raisers involving multi-scale damages such as fibre–matrix debonding, matrix cracking, inelasticity, fibre breaking and delamination. In the particular case of thin woven composites under fatigue loading, only a few works tried to answer this issue [13, 15]. To characterize notch propagation and its effects, different destructive and non-destructive tests can be undertaken. Reference [15] tried to correlate microscopic observations with results

✉ C. Bouvet
christophe.bouvet@isae.fr

[1] Université de Toulouse; INSA, UPS, Mines Albi, ISAE; ICA (Institut Clément Ader), 3, rue Caroline Aigle, 31400 Toulouse, France

[2] Eurocopter, 13725 Marignane, France

obtained with X-ray, ultrasound C-scan imaging, acoustic emission, or digital image correlation techniques. In those latter works [13, 15], a backlighting technique was used to characterize crack propagation in notched composite laminates.

The originality of this present work is the use of infrared thermography (IRT) technique associated with classical micrographic cuts to evaluate the damage growth in thin woven composite laminates. Firstly, the results of a tension test in the fibre axis are briefly presented. These results are taken from a previous published article [7, 8]. This part shows a damage scenario with development of transverse yarn cracking, similar to the cracks observed by [3]. The IRT allowed for an early detection of the occurrence of the transverse matrix cracking and the kinetics of growth. The second part deals with two different shear tests: a classic $\pm 45°$ tension test and rail shear test. These two different types of tests show different damage scenarios, even if the shear stress/strain curves are similar. The $\pm 45°$ tension test shows matrix hardening and matrix cracking whereas the rail shear test shows only matrix hardening. The IRT is used to perform an energy balance and enabled visualization of the portion of dissipated energy caused by matrix cracking.

In all these cases, the IRT allowed to help determine the damage scenario on one hand, and to perform an energy balance on the other hand, in order to evaluate the effect of each damage phenomenon on the total dissipated energy.

The samples used in this study are made of 8-harness satin balanced glass/epoxy (913-45 %-7781) woven fabric prepreg (available from Hexcel Company). The unit cell and the properties of the 8-harness satin glass/epoxy prepreg ply are given, respectively, in Fig. 1 and Table 1. The yarns are elliptical (half width: 0.25 mm and half height: 0.05 mm). 8-harness satin weaves exhibit ply asymmetry: the weft threads cover seven warp threads, and vice versa. Two sides can be distinguished: the weft and warp faces. Furthermore, the weaving points are not aligned to the principal directions of orthotropy but at a direction oriented at 18.4° to the yarn axis. This asymmetry causes out-of-plane strains after curing.

All samples were made with the same (warp or weft) woven face on the top of the thickness. The different stacking sequences used in this study will be noted as follows:

Table 1 Properties of the 8-harness satin glass/epoxy prepreg woven ply

Property	Value
Matrix mass ratio	45 %
Density	1730 kg m^{-3}
Fibre basis weight	303 g m^{-2}
Thread count	22 yarns cm^{-1}
Nominal thickness	0.31 mm

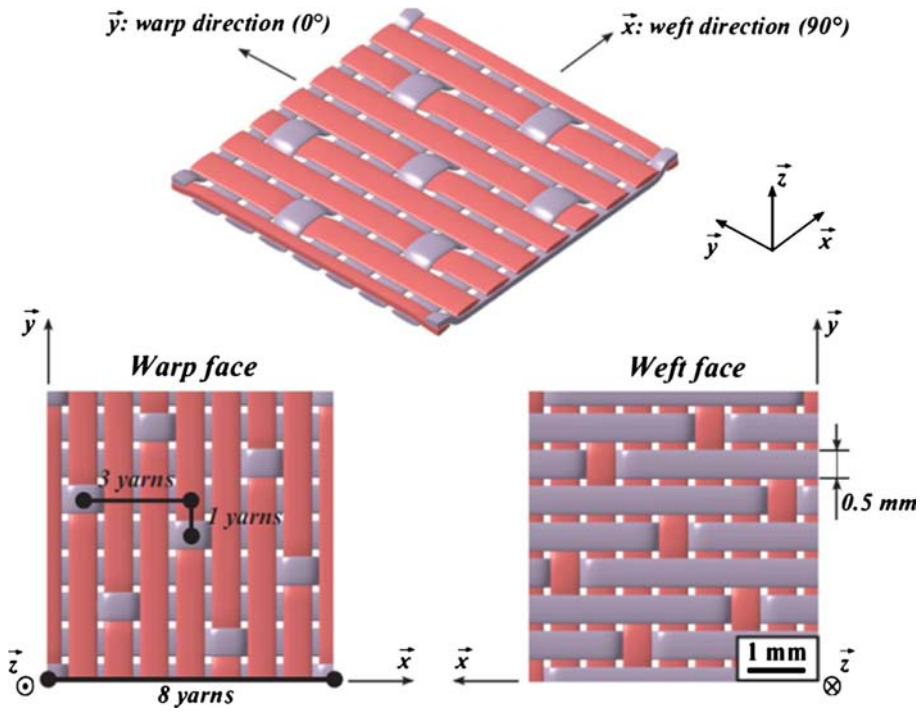

Fig. 1 Unit cell of the 8-harness satin glass/epoxy prepreg ply [7]

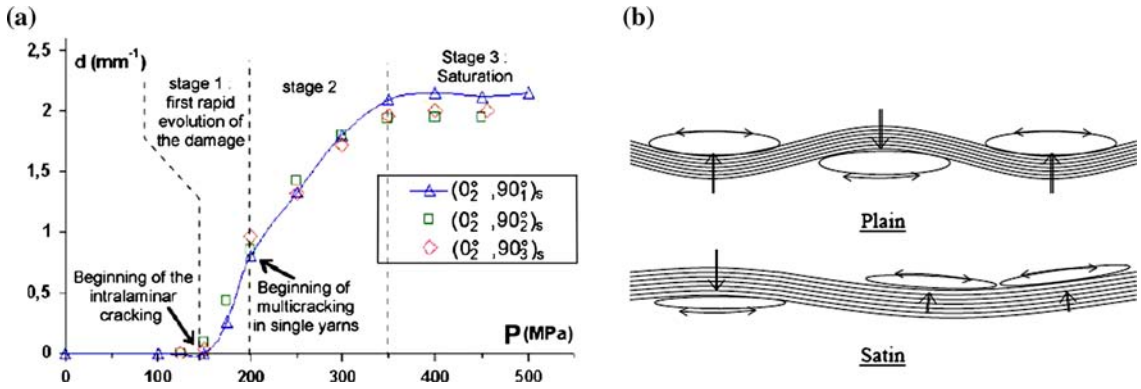

Fig. 2 **a** Changes in cracks density (cracks/mm) in 90° plies for 4-harness satin balanced glass/epoxy $[0_2,90_n]_s$ ($n = 1, 2, 3$) woven composites [19]. **b** Bending loads in the transverse yarns [3]

- n plies stacked in the same direction will be noted as $[0]_n$ when loaded in the warp direction and $[90]_n$ when loaded in the weft direction;
- n plies stacked at ±45° will be noted as $[\pm 45]_n$.

Loadings in fibre axis

The behaviour of woven composites under quasi-static tensile loading along warp or weft direction has been widely discussed in the literature [1–4, 18–20]. It is almost linear until the knee point is reached. This failure point is generally linked to matrix crack extension in the weft yarns [1] due to crack initiation near weaving points [4]. The authors agree that this matrix cracking is linked to waviness in the longitudinal yarns, inducing bending loads in the transverse yarns (Fig. 2). Micro-cracking initiates in those transverse yarns and propagates through the strand thickness. With increasing load, transverse cracks density increases until a specific strain level is reached corresponding to a saturation level (Fig. 2a). Depending on the material structure, the curve bending is more or less important [3, 18] and reached at different levels of the strain. The stiffness reduction is smaller for carbon-fibre-reinforced laminates than for glass-fibre reinforced. Carbon fibres are more rigid than glass fibres. Transverse cracking thus induces less loss of stiffness in the composite. Reference [3] showed that the knee point exhibits a higher strain level for a satin woven laminate than for a plain one (with same components). Yarns waviness is smaller for satin woven composites. This leads to the need for a higher strain to generate bending loads in transverses yarns (Fig. 2b). Furthermore, cracks propagate more widely with satin than with plain woven composites.

Changes in Poisson's ratio and damage mechanisms are also linked to the number of stacked plies. Reference [18] showed a decrease in the stiffness and an increase of the strain level and of residual stresses for 2-ply laminates compared to 4- or 6-ply composites. For 2-ply laminates, transverse cracking appears at lower strain levels and induces changes in the reinforcement's directions leading to a release of the load in transverse yarns. Whatever the number of plies, free edges conditions govern the stress distribution in external plies. Thus, those outer plies highly alter the mechanical properties of 2-ply laminates.

With the strain level increase, transverse cracking propagates, leading to initiation of meta-delamination (delamination at the interface between longitudinal and transverse fibre bundles within a same layer) in weaving areas or even delamination between plies. The final failure of the laminate is linked to the brittle fracture of the fibres (strain levels between 1.5 and 3 % for glass woven fabrics). In the literature most woven composites exhibit the following damage scenario:

1. matrix-fibre debonding and matrix cracking in transverse yarns,
2. meta-delamination in weaving areas,
3. inter-ply delamination, and
4. longitudinal fracture of the fibres.

The same general trends were observed for 2- and 4-ply specimens ($[0]_n$ and $[90]_n$) made of the material of the study and submitted to quasi-static tensile tests [14–16]. So, interrupted tensile tests (on an electromechanical tension machine: INSTRON, capacity: 10 kN) were performed on $[0]_2$ specimens to highlight the damage scenario using micrograph SEM analysis [7]. In-plane (noted A–D) and through-the-thickness (noted A′–D′) observations were obtained at different strain levels: just before the knee point, after the knee point and at the final failure (Fig. 3). As shown in [3], transverse yarn cracking initiates near the knee point (A and A′). With the increase of the strain level, cracks develop within transverse yarns leading to intralaminar fractures. Those cracks are linked to coalescence of fibre–

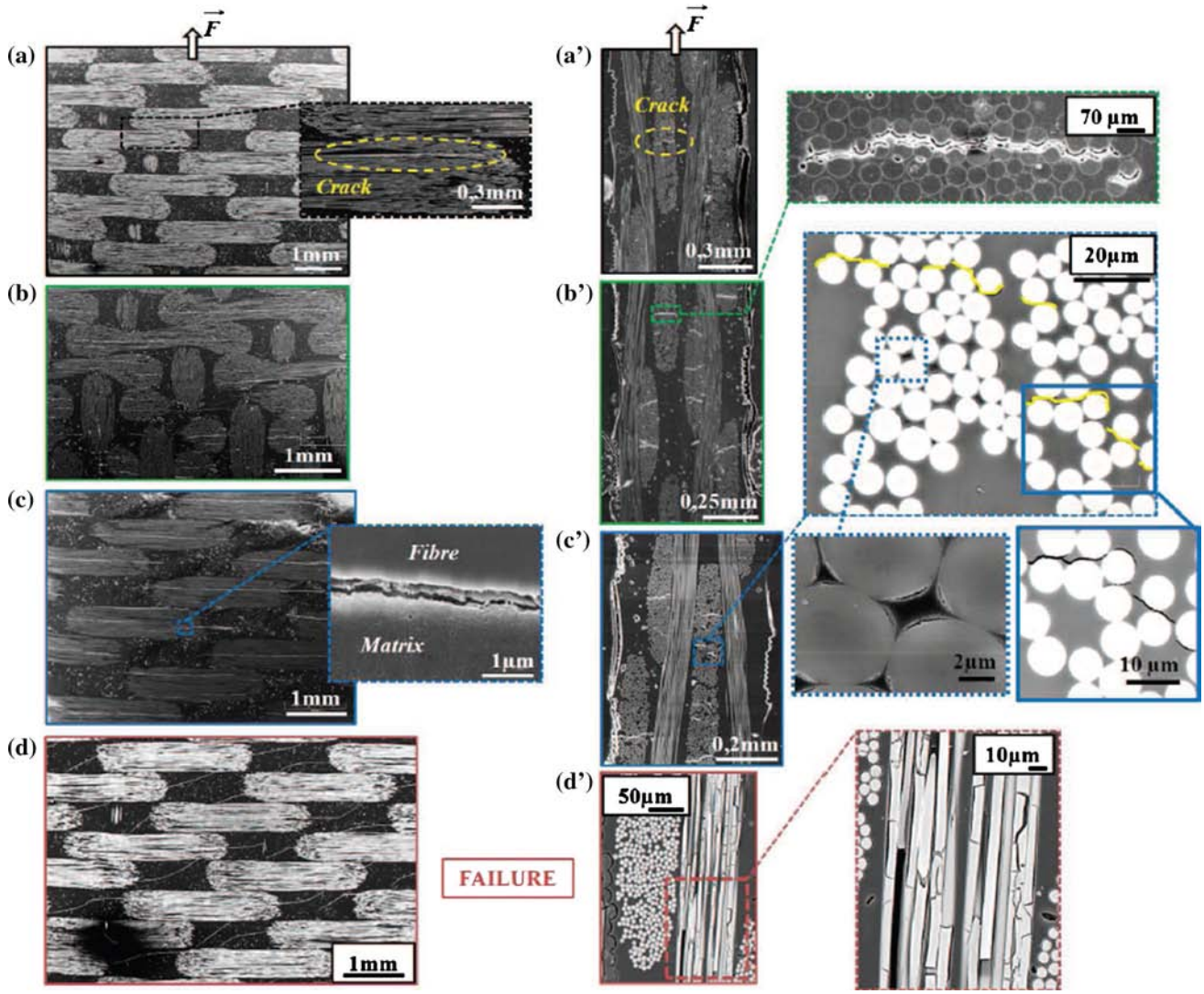

Fig. 3 SEM micrographs at different strain levels: in-plane (*A*–*D*) and through-the-thickness (*A*′–*D*′) observations [7]

matrix debonds (magnification of C′). Cracks extend into the strand thickness direction especially in lower matrix content areas at fibre–matrix interfaces (C, B′ and C′). Then transverse micro-fractures extend toward the cross-over points of the woven plies (D). Multiple fractures were also detected along the warp yarn fibres (D′), which might be due to shock wave propagation induced by the earliest fibre ruptures. The final failure of the specimen is caused by the combination of transverse crack densification, the intersection of several small cracks and the warp fibre ruptures. No meta-delamination was observed even for high strain level (up to 2.2 %). This could be explained by the particular weaving of the 8-harness satin woven fabric. The observed damage scenario can be resumed as follows:

1. fibre–matrix debonding and coalescence leading to strand cracking,
2. transverse yarn cracking extension toward the cross-over points, and
3. macroscopic failure of the laminate due to warp strands breaking.

Infrared measurements were performed on $[0]_2$ samples (both weft and warp faces were monitored) to highlight spatial and temporal damaging during loading (tensile test at 20 mm mn^{-1}). The curve of longitudinal stress σ_y, evaluated by $\sigma_y = \frac{F}{S}$, versus longitudinal strain ε_y, measured using an extensometer, is plotted in Fig. 4a. Samples were painted matt black and enclosed in a rectangular box made of expansive foam to measure the temperature variation field avoiding external thermal perturbations. Heat sources were estimated as described in [7]. The experimental setup was the following:

- image capture frequency: 50 Hz,

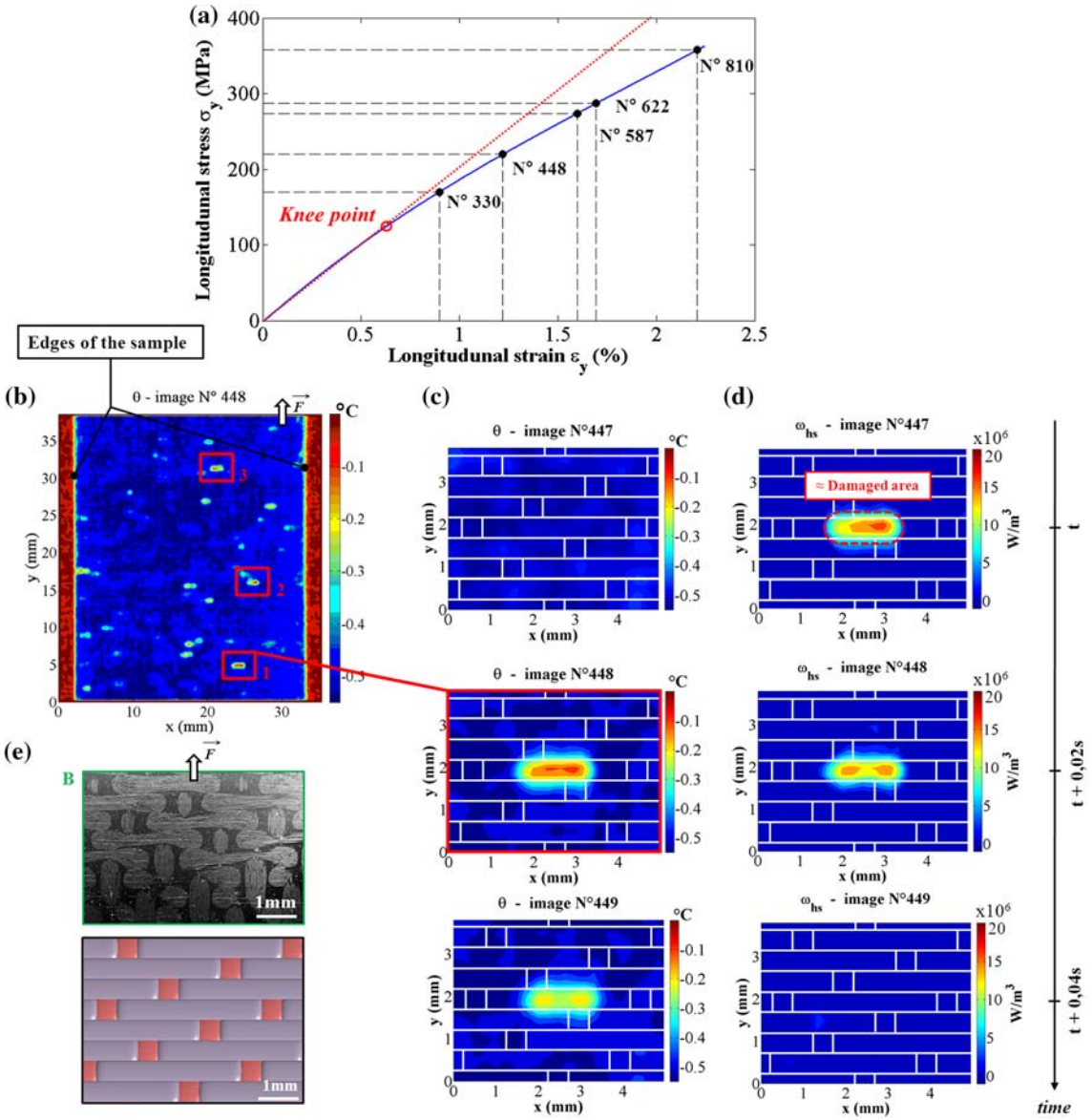

Fig. 4 **a** Stress–strain curve indicating selected pictures; **b** Temperature variation fields of the entire observed zone; **c** Temperature variation fields and **d** corresponding heat source fields with the weave pattern of the layered weft face; **e** SEM micrograph C and schematic representation of the weft face [7]

- thermal resolution: 0.025 K (for relative temperature measurement),
- spatial resolution (pixel size): 0.17 mm (maximum magnification of the lens) in order to have at least 3 pixels per yarn,
- inspection area: 54 × 43 mm^2.

Figure 4b shows the temperature variation field of the weft face zone at a strain level of 1.25 %. Both inspected surfaces undergo quasi-homogeneous cooling due to the thermo-elastic effect at the beginning of loading. On the weft face, several localized increases of temperature appear just after the knee point is reached. The occurrence of those locations multiplies with the loading until a plateau is achieved (strain level of about 1.6 %). This phenomenon is not detected on the warp face but is accompanied by a decrease in the cooling slope. Magnification of one of these thermal patterns and the corresponding heat source (ω_{hs}) field evolution are presented in Fig. 4c and d. The heat source ω_{hs} is defined as the right-hand side of the heat diffusion equation in the absence of an external heat source term:

$$\rho C_p \dot{T} + \mathrm{div}(q) = \omega_{hs} + r_{ext}, \quad (1)$$

where ρ is the mass density, C_p the specific heat capacity, T the temperature, q the heat flux vector and r_{ext} the external volume heat supply which is assumed equal to zero.

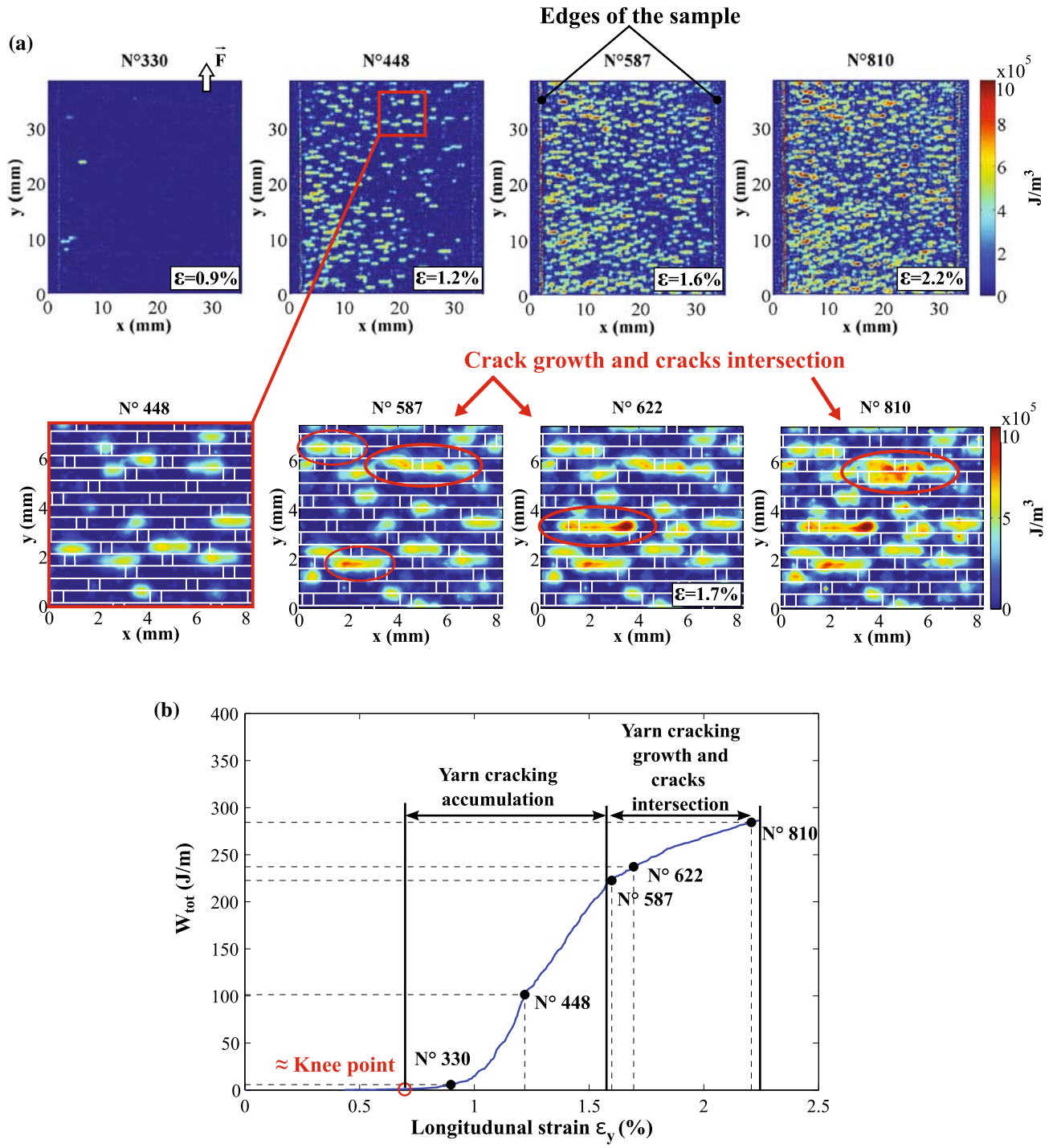

Fig. 5 **a** Temporally accumulated energy E_{tot}; **b** Evolution of the total amount of dissipated energy W_{tot} as a function of longitudinal strain [7]

Compared to SEM micrographs, heat sources can be linked to transverse yarn micro-cracking initiation and extension (Fig. 4). The dissipative heat sources represented in Fig. 4d illustrate that irreversible work develops around the crack over a band slightly greater than the yarn width ($\approx$0.8 mm). A spatial cartography of all the transverse micro-cracks can thus be obtained at any strain level by temporally accumulating experimental heat sources calculated at each image pixel.

Figure 5 presents the total cumulative volume energy E_{tot} (J m^{-3}) cartography at three different levels of strain (Fig. 5a; Eq. 2) and the total amount of dissipated energy by thickness unit throughout the observed zone W_{tot} (J m^{-1}) (Fig. 5b; Eq. 3):

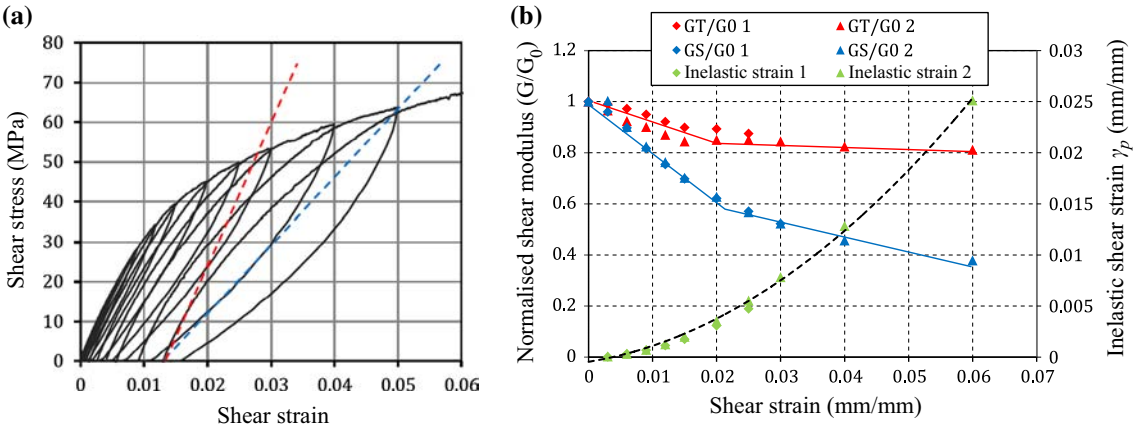

Fig. 6 **a** Shear stress/strain curve of a $[0]_4$ sample (the *dotted red* and *blue lines* represent, respectively, the tangent and secant modulus); **b** Evolution of normalized tangent (GT) and secant (GS) shear modulus, and inelastic strain (Color figure online)

$$E_{\text{tot}}(x,y,t) = \int_0^t \omega_{\text{hs}}(x,y,t)\,\mathrm{d}t, \tag{2}$$

$$W_{\text{tot}}(t) = \int_0^t \int_0^{L_x} \int_0^{l_y} \omega_{\text{hs}}(x,y,t)\,\mathrm{d}x\,\mathrm{d}y\,\mathrm{d}t, \tag{3}$$

where t is the total integration time, and L_x and l_y are the width and length of the processing zone, respectively.

As shown in pictures 330 and 448, transverse yarn cracking initiates around the knee point and accumulates in several weft yarns as strain increases (Fig. 5a). Transverse matrix crack densification occurs essentially between strain levels of 1 and 1.55 % (correlated with the increase in dissipated energy). Afterwards, magnifications of pictures N° 448 to N° 810 show crack extensions as crack intersections between adjacent yarns, leading to a slower accumulation of dissipative work, after a strain level of 1.55 %. Picture N° 810 is correlated to the bifurcation of cracks toward the cross-over points of adjacent yarns observed on the post-mortem micrograph (Fig. 3d). It demonstrates that close to the final failure point, most of the weft yarns exhibit micro-cracks.

Off-axis loading

Introduction

In this part, we consider the characterization of the shear damage of glass/epoxy fabric. For this loading, the behaviour and the mechanisms of degradation of a ply are mainly controlled by the resin. Macroscopic shear behaviour of an orthotropic, unidirectional or woven, ply is generally characterized in the system of orthotropy axes by an off-axis tensile test on a $[\pm 45]_n$ lay-up. It is the most widespread test due to its simplicity of setting-up and analysis. This test was standardized for testing composite materials with polymeric matrix [21]. However, as the stress state does not correspond to a pure shear test, the damage is thus influenced by the tensile components. Moreover, these tensile components in the fibre direction are increased with the fibre reorientation in the load direction, when the deformation becomes large. This phenomenon particularly prevents the measurement of a breaking shear stress or strain. A large number of other in-plane shear test methods exist to characterize in-plane shear behaviour, and Ref. [22] counted more than 30, while preferring the rail-shear test method.

The macroscopic behaviour of the glass/epoxy fabric was previously studied in the laboratory by [15–17], using the off-axis tensile test, and more recently by [14] via a rail shear test. The stress/strain graph of a $[0°]_4$ specimen for a rail shear test is presented in Fig. 6. Shearing behaviour—controlled by the resin—is initially linear then followed, from approximately $\gamma = 0.9$ %, by a nonlinear phase (progressive "strain hardening") where inelastic strains develop [14]. We can also note a hysteresis effect as well as partial relaxation of the inelastic strains at zero stress, translating the typical visco-elastic behaviour of an epoxy resin [23, 24]. Lastly, failure occurs at strains levels that are much higher than when the load is aligned with a fibre axis. The evolutions of the residual strains and the standardized tangential and secant modulus, compared to the initial modulus G_0, are given in Fig. 6b for two different specimens. The initial shear modulus G_0 is estimated at approximately 3.54 GPa by [15] (off-axis tensile test) and 3.82 GPa by [14] (rail shear test). The modulus reduction observed with the criterion of secant modulus (up to 60 %) is higher than with the tangent modulus (20 %). The inelastic strain presents a quadratic evolution according to the total deflection.

In order to give details on the nature and the kinetics of the shear damage, off-axis tensile tests on $[\pm 45]_2$ lay-up are studied using thermal measurements and micrographic cuts. A comparison with a rail shear test is also presented.

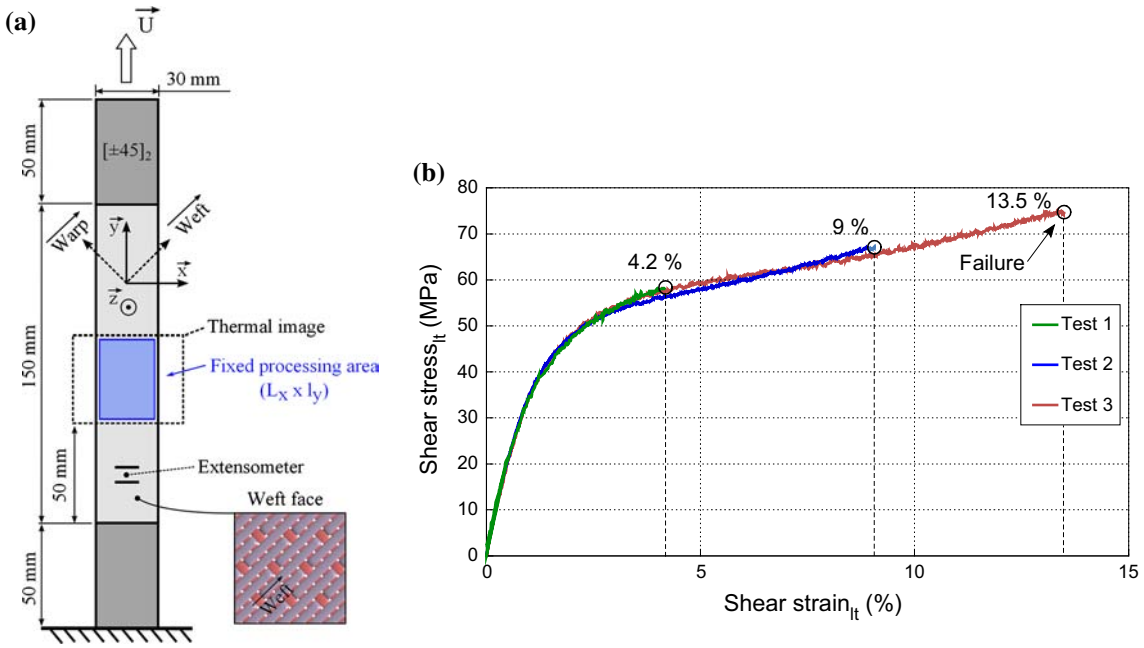

Fig. 7 **a** Geometry of the traction samples $[\pm 45]_2$ and **b** stress/strain curves of different tests

Tensile tests at ±45°

Damage characterization at the microscopic scale

The off-axis tests on $[\pm 45]_2$ laminates were carried out at room temperature and at a constant speed of 40 mm min^{-1}. The specimen geometry (Fig. 7a) is the same one as for the tensile tests in the fibre axis. The shear stress τ_{lt} and the shear strain γ_{lt}, expressed in the system of orthotropy axes, are calculated from the following relations:

$$\tau_{lt} = \frac{\sigma_y}{2} = \frac{F}{2S} \quad \text{and} \quad \gamma_{lt} = \varepsilon_y - \varepsilon_x = (1 + \nu_{xy})\varepsilon_y \tag{4}$$

where F is the tensile load experimentally measured, S is the specimen section, ε_y is the longitudinal strain measured by an extensometer and ν_{xy} is the homogenized total Poisson's ratio ($\nu_{xy} \approx 0.5$ [15]). The curve of shear stress τ_{lt} versus shear strain γ_{lt} is plotted in Fig. 7b for three different tests.

The damage at a microscopic scale is then examined on three specimens loaded at increasing strain levels (Fig. 8). Corresponding micrographic views are presented in Fig. 8a (cut normal to the z-direction) and Fig. 8b (transverse perpendicular cuts to the weft direction). The micrographic views show that no matrix microscopic crack develops up to 4.2 % of shear strain. Comparatively, [23] note the occurrence of these microscopic cracks from 2.27 % for a carbon/epoxy fabric. They specify that they result from the coalescence of multiple fibre–matrix debondings developing at lower strain levels. For a shear strain of around 9 %, several matrix cracks are observed in the warp and weft yarns. The presence of fragments is observed inside these cracks, those occur perhaps because of an important local shear (formation of "cups"). As in 0° tensile test, these cracks are not necessarily initiated at the weaving points and are propagated mainly along the fibre–matrix interfaces. For this strain level, multiple fibre cracks, sometimes in the same fibre, are also observed (Fig. 8a). To 9 % of shear strain, the tensile strain reaches approximately 3 % which is higher than the fabric breaking tensile strain (around 2.2 %). Thus, it is not surprising to observe fibre cracks at this shear strain level.

The post-mortem views (Fig. 8) show that nearly all the yarns are cracked after the total failure of the specimen. Figure 8b shows that these cracks propagate up to the weaving points where they induce meta-delaminations. According to [25], the latter are explained by the occurrence of an out-of plan shear at the fibre points, generated by the yarn swivelling.

Analysis of thermal and heat sources fields

The $[\pm 45°]_2$ tensile tests are performed using IRT (same acquisition frequency, insulating enclosure, etc., as previously described). Only a small area, represented by the blue area on Fig. 7a, is considered for post-treatment of thermal images. The changes in temperature are measured on an area located at the centre of the specimen (Fig. 7a) in order to avoid thermal disturbances near the jaws. Indeed, the yarns that have one end embedded in the tab are affected by a higher tension, resulting in a more significant thermoelastic cooling in the areas near the tabs (Fig. 9).

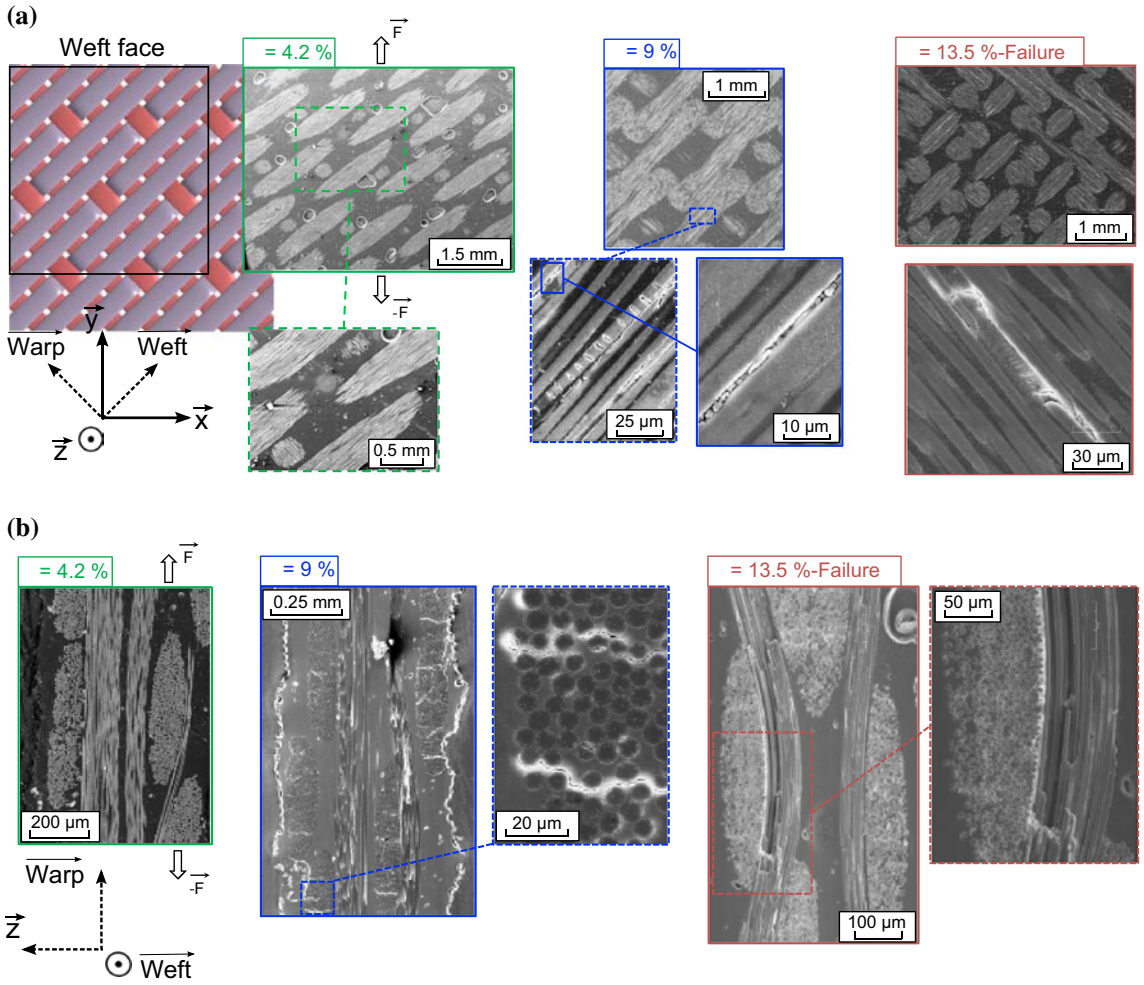

Fig. 8 SEM micrographs at different strain levels: **a** in-plane observation of the weft face and **b** transverse cuts

A temporal filtering is carried out by a low pass filter (FIR: finite impulse response, implemented in Matlab) at the standardized cut-off frequency, $\overline{f_c} = 2f_c/f_e = 0.04$. A space filtering is then carried out by using a square space of $N_x \times N_y = 21 \times 21$ pixels^2. For this configuration, the detectability threshold on the amplitude of the heat sources is estimated at 0.15×10^6 W m^{-3}. Heat sources of lower amplitudes can thus be measured, but the size of detectable spatiotemporal heterogeneities of dissipation will be consequently lower.

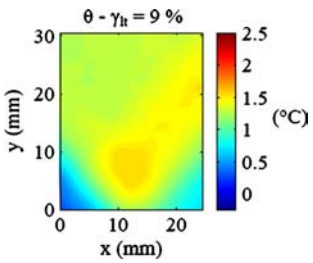

Fig. 9 Temperature field observed in the weft side for a zone situated at 15 mm of the fixed lower grip

The results obtained on weft and warp faces (for two different specimens) are presented in Figs. 10 and 11. The stress/strain curves (Fig. 10) are identical until a shear strain of about 9 %, beyond which the macroscopic behaviours of the two specimens differ slightly. Nevertheless the evolution of the average temperature follows the same trend. The warming of the weft face specimen decreases slightly compared to that observed on the warp face (Fig. 10) around a shear strain of 9 %. The weak difference observed is certainly due to a problem of experimental reproducibility. Let us note that this divergence appears for a strain level where yarn reorientation is observed.

Fields of temperature variation observed for the four strain levels considered during the microscopic analysis are presented on Fig. 11a for the weft face and Fig. 11b for the warp face. For both faces, the thermo-elastic cooling observed until a shear strain of around 1.0 % ($\approx$threshold of plasticity observed by [14–16]) is homogeneous in the area. It is however slightly higher on the weft face, but the variation is relatively weak. A slight change in the ply orientation between the two specimens, due to the manufacturing process, can cause this disparity.

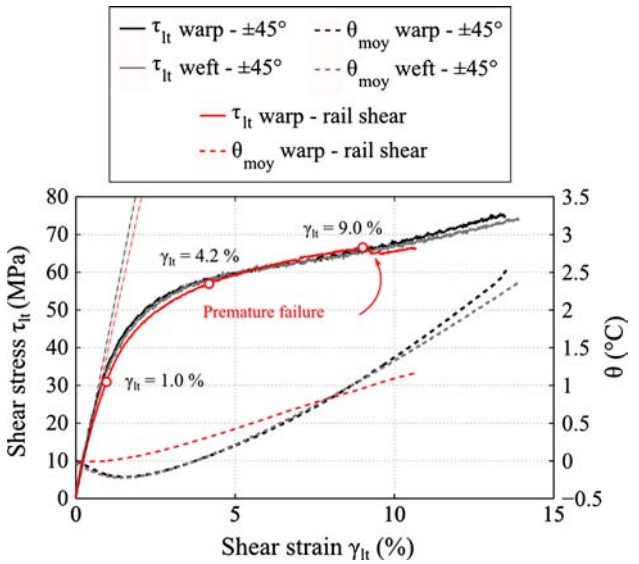

Fig. 10 Stress/strain curve and evolution of the average temperature of two different ±45° tensile tests and a rail shear test

Finally, whatever the observed face, no strong rise in temperature—possibly linked to the occurrence of intralaminar cracks—is obtained during the test. With regard with the linearity loss (Fig. 10, $\gamma_{lt} \approx 1$ %), it can be deduced that the spatial distribution of the temperature variation is influenced by the yarn orientation (Fig. 11a, b). On the contrary, the distribution of the heat sources is "random" and does not present any privileged direction (Fig. 11c for the weft face and Fig. 11d for the warp face).

However, the interpretation of these source fields remains complex because of a significant amount of temporal noise. Figure 12a shows that the average temporal evolution of the heat source calculated on one pixel is strongly disturbed: negative (thermo-elastic effect) and positive sources are observed. The temporal evolution of the heat source fields according to the A profile (Fig. 11c) confirms this progressive increase in the heat source intensity even if a space noise of weaker frequency is observed (Figs. 11b and 12c).

The intensity of the heat sources is approximately 10 times lower than when the specimen is loaded in the fibre axis. In addition, no localized source appears. This shows that the few observed intralaminar cracks exhibit an energy too low to be detected. The intensity of the heat sources being linked to the rate loading tests led to higher rate loadings could possibly reveal these micro-cracks. Of course, this is true only if their thermal demonstrations are not too weak compared to that induced by the pseudo-strain hardening of the resin.

Finally, dissipative source fields with amplitude lower than 10^6 W m^{-3} seem mainly linked to the progressive "pseudo-strain hardening" of the resin. Indeed, even if they are highly noisy, their evolutions seem to indicate the development of progressive dissipative source fields. The occurrence of intralaminar shear cracks, caused by the coalescence of fibre–matrix debondings, seems less brutal compared to the tensile cracks observed on $[0°]_2$ lay-up. Contrary to the tests in the fibres axis, results obtained on the two faces reveal a low heterogeneity of the various fields in the thickness direction. The assumption of a homogenous distribution of the temperature and the source fields through the thickness seems reasonable here.

Rail shear tests

The specimens warp face is filmed during rail shear tests to observe the influence of the hydrostatic tensile component—inherent in the off-axis tensile test—on the material shear damage mechanisms. The rail shear apparatus developed to avoid local shear buckling by [14] is used on a hydraulic tension machine to perform tests on $[0]_4$ specimens (Fig. 13). The shear strain is measured using a modified extensometer with vertical knives [14].

The moving clamp (Fig. 13a) is moved at 3 mm min^{-1}, which corresponds to a rate of shear strain ($\approx 0.8 \times 10^{-3}$ % s^{-1}) approximately 8 times lower than the shear strain rate obtained during the off-axis tensile tests ($\approx 6.7 \times 10^{-3}$ % s^{-1}). The comparison of the stress/strain graphs (Fig. 10) shows a good correlation between the two tests until a shear strain of approximately 9 %. From this strain level, a stiffening generated by the fibre reorientation appears on the $[\pm 45°]_2$ specimens, and a premature shear breaking of the specimens occurs in the specimen corners near the embedded edges. Figure 14 presents a micrograph cut (MEB) obtained for a shear strain of 7.2 %. At this value, inelastic strains and stiffness reduction are observed by [14], whereas the material does not present any damage on a microscopic scale. Indeed, no resin micro-cracking or "crazing" is observed. This failure mode occurs in areas exhibiting important hydrostatic strain or strong localized plasticity. This phenomenon is due to development of 10-nm diameter micro-porosities propagating perpendicular to the tensile direction until a crack is created [26]. The crack planes are then connected by a fibril network (polymer fibre made up of several macromolecular yarns) of a few nanometres in diameter. If the damage occurs on such a scale, it cannot be detected using the current method. These observations are consistent with those of [14] that shows only some isolated microscopic cracks for a cyclic loading, which is insufficient to justify the degradation of the macroscopic behaviour. This behaviour differs from the ±45° tensile behaviour where micro-cracking appears for lower strains (Fig. 8). Reference [27] showed through several tests (traction, compression, shear) that the epoxy resin behaviour and its failure mode strongly varied according to the amplitude of the hydrostatic part of the stress tensor. The authors show that when the hydrostatic part is important (tensile test), the resin presents a

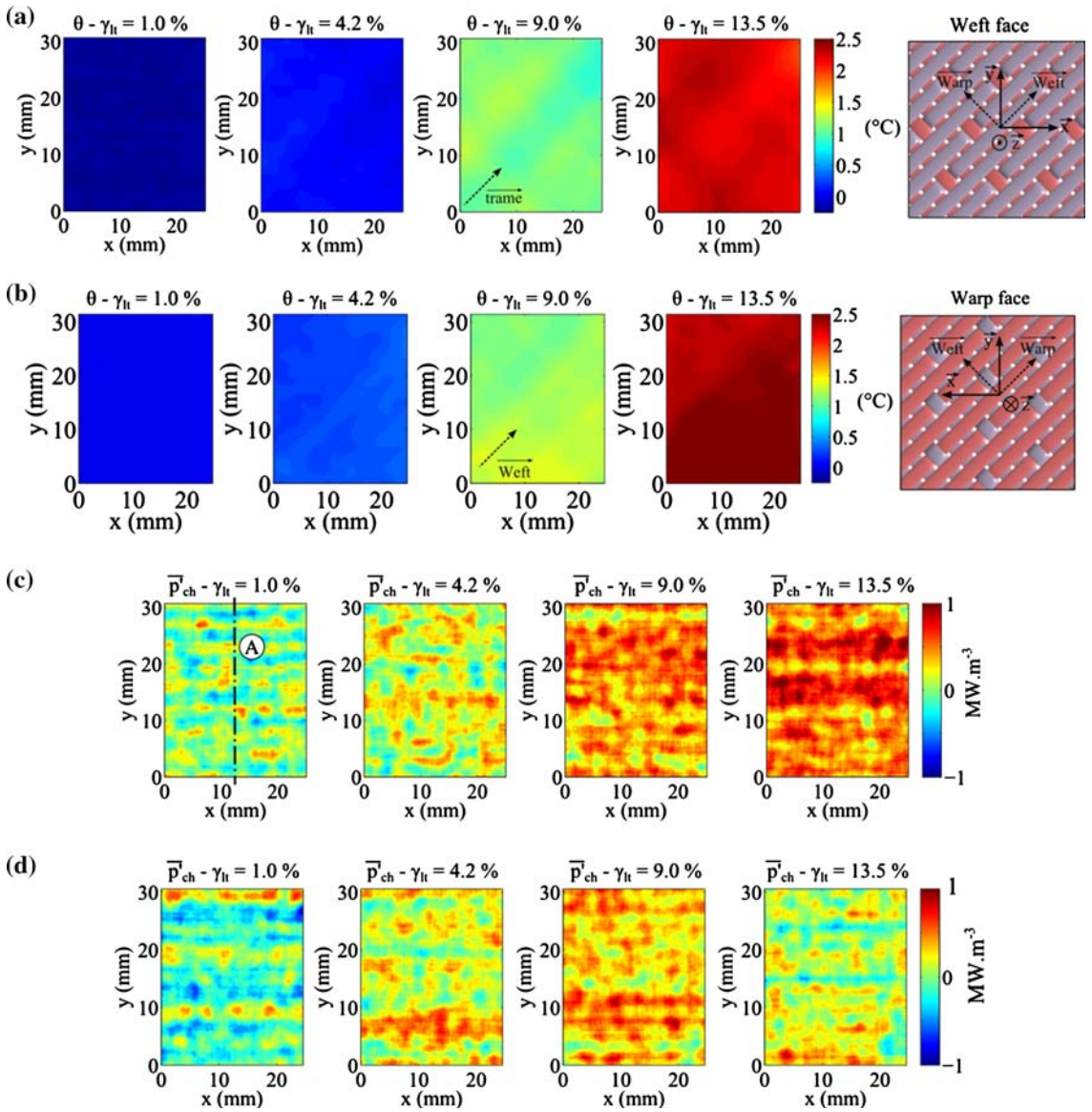

Fig. 11 Temperature field of **a** weft face and **b** warp face, and heat source field of **c** weft face and **d** warp face for different shear strain levels

brittle behaviour and failure mode, whereas in the contrary case (shear test) it behaves like a ductile material and breaks due to large plastic deformations. They explain, from the fracture topography observation of the various samples, why the hydrostatic stress would be responsible for the microscopic crack nucleation and that the deviatoric part would control the plastic behaviour. The resin cracking is thus strongly influenced by the triaxial stress state in material. It could explain the difference between the ±45° tensile tests (considerable hydrostatic part) and the rail shear test (almost nonexistent hydrostatic part).

The change in the average temperature on the warp face are plotted in Fig. 10. Contrary to the off-axis tensile tests, no thermo-elastic cooling phase is observed during the elastic linear phase. The temperature variation is equal to zero. For a level of strain of approximately 0.9 %, the temperature increases linearly until the appearance of the early failures on the specimen edges where the test is stopped (Fig. 10). Taking into account the previous micrographic observations (no micro-crack), this increase represents the heating generated by the "pseudo-strain hardening" of epoxy resin in shear. This heating is comparatively weaker than the one observed during the ±45° tensile tests, but more homogeneous (Fig. 15a).

The heat source fields are estimated by keeping the parameters of the filtering method used for the ±45° tensile tests. The observation is identical to the off-axis tensile tests; the noise present on the source fields does not allow to represent the spatial distribution of the heat sources with sufficient precision (Fig. 15b). Moreover, the source intensity is

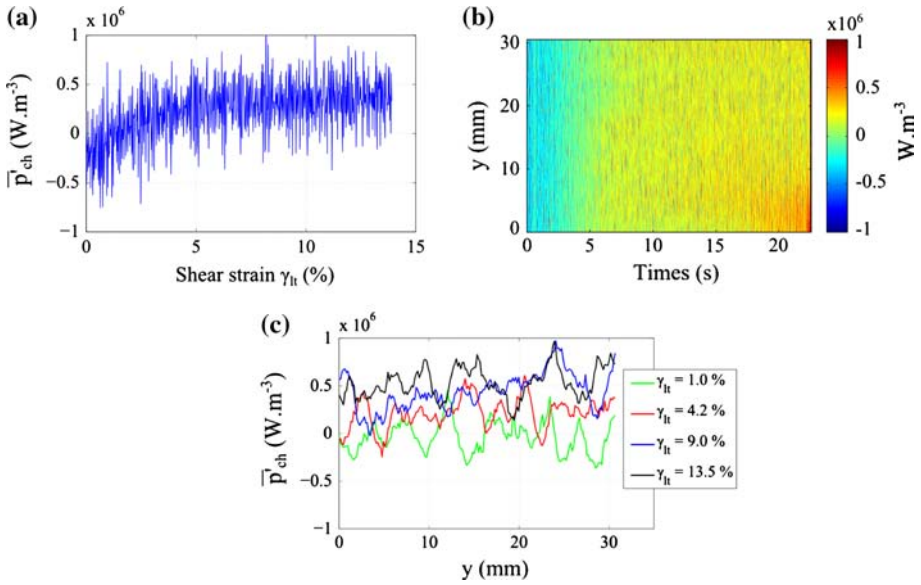

Fig. 12 **a** Evolution of the heat source evaluated weft side for a pixel situated at the sample centre; **b** Evolution of the heat sources along the A profile defined Fig. 11c; **c** Distribution of heat sources along the A profile at different shear strain levels

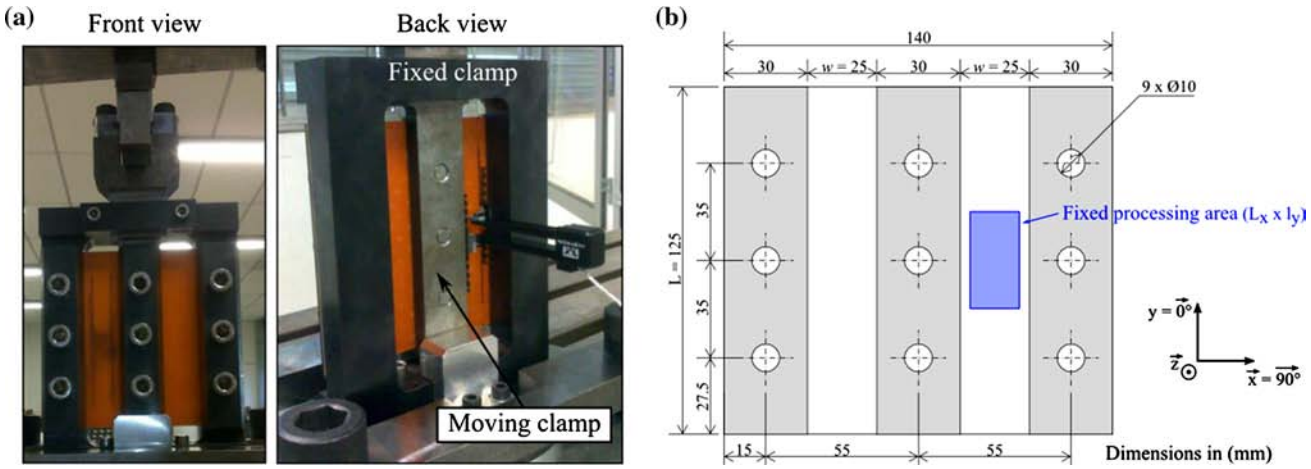

Fig. 13 **a** Experimental set-up of the rail shear test and **b** geometry of the associated sample [13]

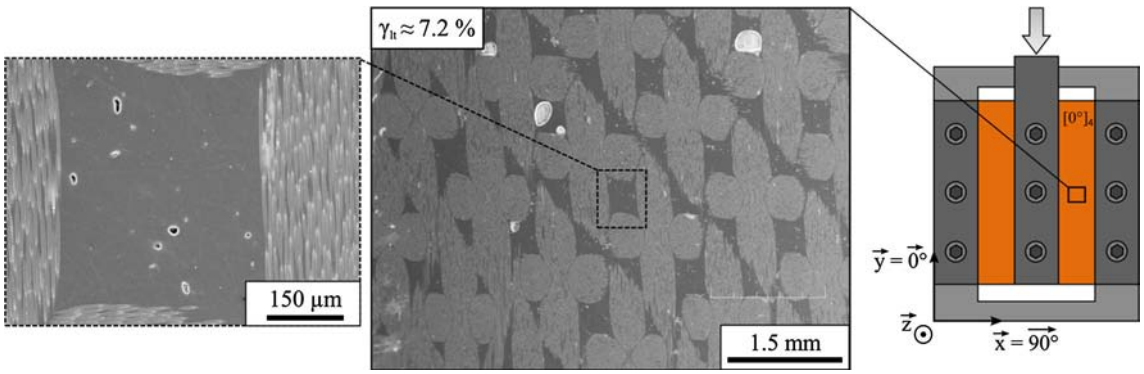

Fig. 14 SEM micrograph of the warp face for 7.2 % of shear strain level

lower than those observed during the ±45° tensile tests (1 MW m^{-3} for the ±45° traction test against 0.1 MW m^{-3} for the rail shear test). This lower value is of course mainly due to the lower strain rate (6.7 × 10^{-3} % s^{-1} for traction ±45° against 0.8 × 10^{-3} % s^{-1} for the rail shear test). As for the off-axis tensile test, the appearance of positive average heat

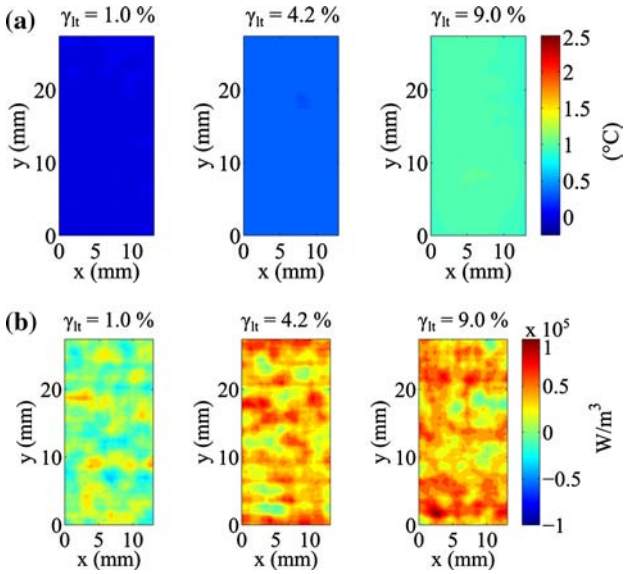

Fig. 15 **a** Temperature field and **b** heat sources at different shear strain levels of the rail shear test

sources on surface corresponds to the occurrence of resin pseudo-strain hardening.

In conclusion, the micro-cracks on the off-axis tensile tests cause a calorific dissipation increase which is surprisingly similar to the pure shear test where no micro-crack is observed. A more precise study of the balance of the different dissipated energy types is necessary to explain this phenomenon.

Balance of dissipated energy

The objective of this section is to characterize the ratio of mechanical energy dissipated as heat by the inelastic resin shear using the source fields and mechanical measurements (load, displacement, strain). For this, a quantitative estimation of the energy dissipation is required.

Given the similarity of source fields and temperature observed for both sides of the woven fabric during ±45° tensile test and rail shear test, it seems reasonable to consider that the heat source field observed in one face is quantitatively representative of the one through the thickness. Indeed shear damage being mainly controlled by the resin behaviour, the pseudo-strain hardening can thus be considered constant through the thickness. So the dissipated energy can be evaluated from the heat sources previously evaluated. For off-axis tensile tests, the magnitude of the thermo-elastic source ($\approx 1 \times 10^{-6}$ W m^{-3}) is comparable to that of dissipative heat sources, and therefore cannot be neglected. Taking the latter into account, and supposing the system is balanced at each instant and the kinetic energy is neglected, the energy balance for the two tests can be rewritten as follows:

$$W_{\text{ext}} = W_{\text{r}} + W_{\text{irr}} = W_{\text{r}} + W_{\text{s}} + W_{\text{d}}, \tag{5}$$

where W_{ext} is the external mechanical energy divided in a reversible part W_{r} and an irreversible part W_{irr}.

The irreversible energy W_{irr} is divided in a stored part W_{s} and a dissipated part W_{d}. This dissipated part is the double integral of the intrinsic dissipation ϕ_{int} over time t and over the considered volume Ω:

$$W_{\text{d}} = \int_0^t \int_\Omega \phi_{\text{int}} \, \mathrm{d}\Omega \, \mathrm{d}t. \tag{6}$$

The intrinsic dissipation can be evaluated using IRT and the heat diffusion equation:

$$\rho C_p \dot{T} + \operatorname{div}(q) = \omega_{\text{hs}} + r_{\text{ext}} = \phi_{\text{int}} + p_{\text{the}} + r_{\text{ext}}, \tag{7}$$

where p_{the} is the thermo-mechanical coupling and r_{ext} is the external volume heat supply which is supposed equal to zero.

The temperature variation induced by the occurrence of damage is assumed to be too small to modify the internal state of the material. In this context, couplings between temperature and internal variables are thus insignificant and the thermo-mechanical coupling is assumed to be reduced to the thermo-elastic coupling. Moreover, the thermo-elastic source p_{the} is calculated assuming that the weft and warp sides of the woven fabric behave as a unidirectional ply oriented at +45° or −45°. By adopting the classical laminate theory, the expression of the thermo-elastic source is given by [28]

$$p_{\text{the}} = T\left[\alpha_1(Q_{11} + Q_{12}) + \alpha_2(Q_{12} + Q_{22})\right] \frac{\dot{\varepsilon}_x + \dot{\varepsilon}_y}{2}, \tag{8}$$

where Q_{ii} are the terms of the stiffness matrix expressed in the reference ply frame, α_i are the coefficients of thermal expansion and $\dot{\varepsilon}_x$ and $\dot{\varepsilon}_y$ are the strain rates as transverse and longitudinal directions of the specimen, respectively, estimated from experimental measurements of strain. The parameters used for calculating p_{the} are summarized in Table 2.

For ±45° tensile tests, the temperature variations remain homogeneous and similar on both sides of the woven fabric during the elastic linear phase (Fig. 11). Therefore, thermo-elastic source fields are assumed to be homogeneous through the thickness and on the surface of the observed specimen. The thermo-elastic energy W_{the} is then estimated from the following relationship:

$$W_{\text{the}} = \int_0^t \int_\Omega p_{\text{the}} \, \mathrm{d}\Omega \, \mathrm{d}t = eS \int_0^t p_{\text{the}} \, \mathrm{d}t, \tag{9}$$

Table 2 Properties of the 8-harness satin glass/epoxy prepreg woven ply, from [28]

Material parameters	
Longitudinal Young modulus, E_1 (GPa)	36.8
Transverse Young modulus, E_2 (GPa)	8.4
Poisson's ratio, ν_{12}	0.25
Poisson's ratio, ν_{21}	0.05
Longitudinal coefficient of thermal expansion, α_1 (K^{-1})	6.10^{-6}
Transverse coefficient of thermal expansion, α_2 (K^{-1})	35.10^{-6}

where e is the thickness of the sample and S is the specimen surface considered for the post-processing of the thermal images. The different energy types are then respectively estimated from the following relationships:

- the external mechanical energy W_{ext}:

$$W_{ext} = \int_0^t \int_\Omega \sigma : \dot{\varepsilon}\, d\Omega\, dt = \int_0^t F \cdot \dot{U}_{imp}\, dt, \tag{10}$$

where F and U_{imp} are, respectively, the measured load and the imposed displacement.

- the reversible energy W_r:

$$W_r = \int_0^T \int_\Omega \sigma : \dot{\varepsilon}^e\, d\Omega\, dt = \begin{cases} \text{traction } \pm 45° : eS \int_0^t \dfrac{F \cdot \dot{F}}{S_{45}^2 E_y} dt \\ \text{rail shear test} : eS \int_0^t \dfrac{F \cdot \dot{F}}{S_{cis}^2 G_0} dt \end{cases}, \tag{11}$$

where S_{45} is the initial section of the tensile ±45° specimen: $S_{45} = l \times e$ with l the width of the specimen; and S_{cis} is the initial section of the rail shear specimen: $S_{cis} = 2 \times L \times e$ with L the height of the shear test (Fig. 13b). Finally, E_y is the initial Young's modulus of the longitudinal tensile specimen and G_0 is the initial shear modulus. Note here that the terms established in Eq. 11 assume that the fields stress σ and strain ε^e are considered homogeneous across the zone Ω.

The characterization tests conducted by [14] showed that the shear modulus decreases with shear strain (Fig. 6b), due to damage. In addition, the occurrence of hysteresis loops observed during cyclic tests makes it difficult to estimate shear elastic modulus and therefore the elastic energy put in. Subsequently, the authors assume as a first approximation that the shear modulus remains constant and equal to the initial modulus G_0 during the test, resulting in a slight underestimation of the elastic energy put in.

- the dissipated energy W_d:

$$\begin{aligned} W_d &= \int_0^t \int_\Omega \phi_{int}\, d\Omega\, dt \\ &= \int_0^t \int_\Omega (\rho C_p \dot{T} + \mathrm{div}(q) - p_{the})\, d\Omega\, dt. \end{aligned} \tag{12}$$

Then the stored energy can be evaluated using Eq. 5.

As the sizes of the surfaces considered for post-processing of thermal data depend on the test, we compare the average energy quantities (compared to the volume of study) of each test, denoted $\bar{W}$. Figure 16 shows the evolution of different energy densities depending on the shear strain γ_{lt} for a ±45° tensile test observed weft side.

In this figure, $\bar{W}_{hs}$ represents of course the average energy quantity of the supply energy W_{hs} which is defined as

$$W_{hs} = \int_0^t \int_\Omega \omega_{hs} d\Omega\, dt = W_d + W_{the}. \tag{13}$$

The irreversible energy increases almost linearly from $\gamma_{lt} \approx 1$ %. It is almost half dissipated as heat to about 6.5 % of shear strain. Afterwards, the dissipated energy increases markedly while the stored energy increases slowly, reflecting a change in the degradation mechanism. This change could be due to the development of intralaminar cracking since to about 4 % of shear strain, no cracking is detected (Fig. 8).

A comparison of the energy W_{irr}, W_s and W_d obtained from tensile test and rail shear test is presented in Fig. 17 versus the permanent shear strain γ_p. The evolution of the volume irreversible mechanical energy (inelastic energy) is similar for tensile and rail shear tests. It increases nearly linearly versus the inelastic deformation (Fig. 17a).

In spite of the fact that the irreversible energy is similar for both tests, the rail shear test dissipates less heat energy density compared to the tensile test. As previously

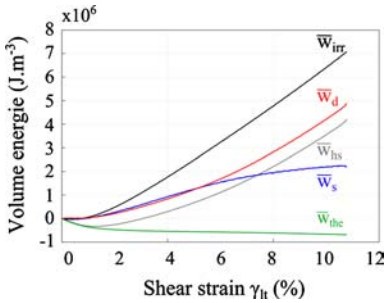

Fig. 16 Energy balance of a ±45° tension test observed warp face

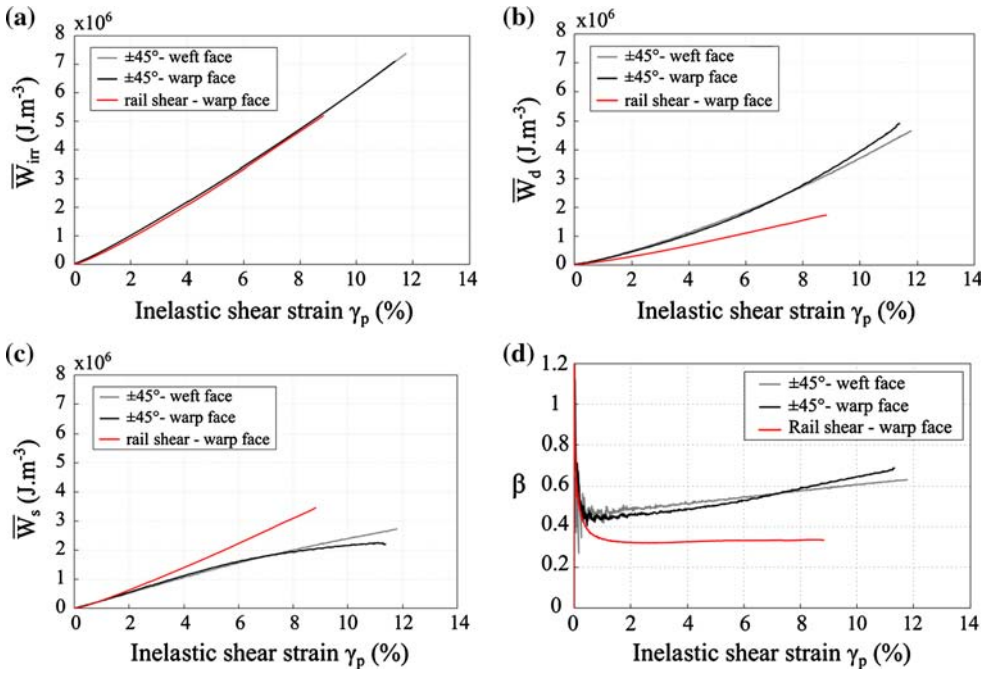

Fig. 17 Comparison between the ±45° tension test and the rail shear test of **a** the irreversible energy, **b** the dissipated energy, **c** the stored energy and **d** the β coefficient

mentioned, a larger dissipation is obtained for the off-axis tensile test due to the development of micro-cracks in the transverse bundles.

Figure 17c shows a comparison between the evolutions of the stored energy densities. The evolution of irreversible energy being similar between the two types of tests, the stored energy density is logically superior for the shear test ($W_s = W_{irr} - W_d$). As previously mentioned, for the same material and the same mechanical energy (which is the case here), a purely pseudo-plastic process tends to store more energy than a process combining brittle damage and inelasticity; this is consistent with the observation of a less dissipative process like the rail shear test. Concerning the off-axis tensile tests, whatever the viewing side, the evolution of the different energy densities remains similar up to about 8 % of inelastic strain which coincides with the apparition of the phenomenon of stiffening due to bundle reorientation. The similarity between the energy dissipated on the two sides of the woven fabric supports the assumption of homogeneous source fields throughout the thickness.

Then Taylor–Quinney coefficient β [10] can be evaluated as the ratio between the dissipated energy W_d and the irreversible energy W_{irr}:

$$\beta = \frac{W_d}{W_{irr}}. \tag{14}$$

Variations of the Taylor–Quinney coefficient, as a function of the permanent deformation, are given in Fig. 17d for the various tests. Reminder, this coefficient is the ratio of energy dissipated as heat to irreversible energy, and of course is less than 1. For small inelastic deformations ($\gamma_p < 1$ %), oscillations and values abnormally higher than 1 are found. Of course, this result is impossible and should result from the inability of the experimental method to evaluate the dissipation energy for low amplitude of deformation coinciding with the beginning of the resin hardening with accuracy. For the shear test, the value of β remains almost constant around 0.33. For tensile tests, the initial value of β is higher ($\beta \approx 0.45$) and increases with increasing inelastic strain until $\beta \approx 0.7$ for the weft side. The linear evolution of β for off-axis traction means that the proportion of energy dissipated as heat increases with the shear strain. The accumulation of heat dissipation due to micro-cracks observed in micrographic pictures seems to explain this trend. These results show that for a pure shear, the ratio of energy dissipated as heat by the resin hardening is lower compared to the case when it is subjected to a part of hydrostatic pressure leading to the appearance of micro-cracks.

Finally, few references are available in the literature on the values of β for epoxy resins. We can still quote the work of [29] who observed that during dynamic tests with Hopkinson's bars ($\dot{\varepsilon} \approx 2500\ s^{-1}$), the values of β are around 0.15. Although the values obtained in this work are not comparable, this study demonstrates that the β ratio depends on different parameters, such as the strain level, the strain rate and the damage mechanisms involved. However, for a laminate with thermosetting epoxy matrix, it seems reasonable to consider the evolution of β is constant during a test if the behaviour is mainly driven by the resin hardening. For the considered shear test, the average value of the β ratio is about 0.33. When the behaviour is governed by some

processes more or less dissipative, the evolution of β is no longer constant and depends on the ratio of energy dissipated or stored by each degradation process.

Conclusion

Although the $\pm 45°$ tensile test and the rail shear test generate a similar macroscopic response, the damage and the dissipated energies scenario differ. Indeed the micrographic observations revealed that the induced hydrostatic pressure by the off-axis tensile test leads to a more "brittle" behaviour of the resin resulting in the occurrence of interface debonding, intra-bundle cracking, meta-delamination and fibre breakage. Such damage is not observed when the resin is subjected to "pure" shear during the rail shear test. These results are consistent with the observations of [27] showing that the macroscopic behaviour of the resin is strongly related to the stress state and particularly in terms of hydrostatic pressure.

From some assumptions, mechanical and thermal measurements were then used to estimate, for both tested configurations, the different input energy quantities. The results have shown that especially when the resin is subjected to pure shear, a larger amount of energy is stored by the material. For the considered epoxy resin, the energy is likely stored inside cracks below the microscopic scale during the hardening process. Furthermore, if the resin undergoes a hardening only (without damage), the change in the ratio of the stored energy can be assumed constant with the increase of the shear strain ($\beta \approx 0.33$). If the hydrostatic pressure leads to micro-cracking of fibre–matrix interface, the stored energy ratio becomes smaller. This result is logical because a purely brittle cracking process dissipates the entire irreversible mechanical energy as heat ($\beta = 1$). Finally, it is not surprising to obtain lower β value for the rail shear test compared to the off-axis tensile test.

Even if this study should be confirmed with further experiments, it shows the interest of using IRT to determine the damage scenario of a composite laminate or to perform an energy balance in order to evaluate the effect of each damage phenomenon on the total dissipated energy.

Acknowledgements The authors wish to thank the "Ecole Nationale d'Ingénieur de Tarbes" for the loan of the infrared camera.

References

1. Pandita SD et al (2001) Tensile fatigue behaviour of glass plain-weave fabric composites in on- and off-axis directions. Compos A 32(10):1533–1539
2. John S et al (2001) Longitudinal and transverse damage taxonomy in woven composite components. Compos B 32(8):659–668
3. Osada T et al (2003) Initial fracture behavior of satin woven fabric composites. Compos Struct 61(4):333–339
4. Daggumati S et al (2010) Local damage in a 5-harness satin weave composite under static tension: part I—experimental analysis. Compos Sci Technol 70(13):1926–1933
5. Vieille B et al (2014) Influence of matrix toughness and ductility on the compression after impact behavior of woven-ply thermoplastic and thermosetting composites: a comparative study. Compos Struct 110:207–218
6. Soumahoro Z (2005) Etude du couplage thermomécanique dans la propagation dynamique de fissure. Université à Palaiseau, Ecole Polytechnique, Palaiseau
7. Lisle T et al (2013) Damage analysis and fracture toughness evaluation in a thin woven composite laminate under static tension using infrared thermography. Compos A 53:75–87
8. Lisle T et al (2015) Measure of fracture toughness of compressive fiber failure in composite structures using infrared thermography. Compos Sci Technol 112:22–33
9. Freund LB, Hutchinson JW (1985) High strain-rate crack-growth in rate-dependent plastic solids. J Mech Phys Solids 33(2):169–191
10. Taylor GI, Quinney H (1934) The latent energy remaining in a metal after cold working. In: Royal society A: mathematical, physical and engineering sciences
11. Rittel D (1999) On the conversion of plastic work to heat during high strain rate deformation of glassy polymers. Mech Mater 31(2):131–139
12. Li ZH, Lambros J (2001) Strain rate effects on the thermomechanical behavior of polymers. Int J Solids Struct 38(20):3549–3562
13. Benevolenski OI et al (2003) Mode I fracture resistance of glass fibre mat-reinforced polypropylene composites at various degree of consolidation. Compos A 34(3):267–273
14. Rouault T et al (2013) Reversible rail shear apparatus applied to the study of woven laminate shear behavior. Exp Mech 53(8):1–12
15. Bizeul M (2009) Contribution à l'étude de la propagation de coupure en fatigue dans les revêtements composites tissés minces. Université de Toulouse, Toulouse
16. Bizeul M et al (2011) Fatigue crack growth in thin notched woven glass composites under tensile loading. Part I: experimental. Compos Sci Technol 71(3):289–296
17. Bizeul M et al (2011) Fatigue crack growth in thin notched woven glass composites under tensile loading. Part II: modelling. Compos Sci Technol 71(3):297–305
18. Gao F et al (1999) Damage accumulation in woven-fabric CFRP laminates under tensile loading: part 1. Observations of damage accumulation. Compos Sci Technol 59(1):123–136
19. Kergomard YD et al (2010) Intralaminar and interlaminar damage in quasi-unidirectional composite structures: experimental analysis. Compos Sci Technol 70(10):1504–1512
20. Alif N, Carlsson LA (1997) Failure mechanisms of woven carbon and glass composites. ASTM Spec Tech Publ 1285:471–493
21. D3518/D3518M-13, 2001 Standard test method for in-plane shear response of polymer matrix composite materials by tensile test of a $\pm 45°$ laminate. ASTM International
22. Lessard LB, Eilers OP, Shokrieh MM (1997) Modification of the three-rail shear test for composite materials under static and fatigue loading. ASTM Spec Tech Publ 1242:217–233
23. De Greef N, Gorbatikh L, Lomov SV, Verpoest I (2011) Damage development in woven carbon fibre/epoxy composites modified with carbon nanotubes under tension in the bias direction. Compos A 42(11):1635–1644
24. Couégnat G (2008) Approche multiéchelle du comportement mécanique de matériaux composites à renfort tissé. Université Sciences et Technologies-Bordeaux I, Bordeaux

25. Karahan M (2011) Investigation of damage initiation and propagation in 2 × 2 twill woven carbon/epoxy multi-layer composites. Text Res J 81(4):412–428
26. Lemaignan C (2003) La Rupture des matériaux. Les Ulis (Essonne), EDP sciences
27. Fiedler B et al (2001) Failure behavior of an epoxy matrix under different kinds of static loading. Compos Sci Technol 61(11): 1615–1624
28. Emery TR et al (2008) A generalised approach to the calibration of orthotropic materials for thermoelastic stress analysis. Compos Sci Technol 68(3–4):743–752
29. Trojanowski A, Ruiz C, Harding J (1997) Thermomechanical properties of polymers at high rates of strain. J Phys IV France 7(C3):447–452